



ASSESSMENT OF IN-DUCT FAN BROADBAND NOISE MEASUREMENTS IN A MODERN LOW-SPEED TEST RIG

Lukas KLÄHN, Antoine MOREAU, Luciano CALDAS, Ulf TAPKEN

*German Aerospace Center (DLR), Institute of Propulsion Technology, Engine
Acoustics Department, Müller-Breslau-Str. 8, 10623 Berlin, Germany*

SUMMARY

The rotor-incoherent components of the sound field emitted by a fan stage in an aeroacoustic fan test rig are analyzed by means of a radial mode analysis with a combined axial and azimuthal sensor array. The resulting sound power is separated into broadband components and narrowband components around the blade passing frequencies, which are not to be confused with pure tones. The trends of the broadband components are linked to the blade loading and flow coefficient. The narrowband components, that are associated with elongated ingested turbulence, are reduced by a honeycomb. Measurements are compared to simulated data obtained from a physics based analytical noise prediction model and to results obtained for a different test rig.

INTRODUCTION

In the analysis of the acoustic components it is often distinguished between tonal and broadband noise. Important broadband noise sources arise from the interaction of turbulent flow with solid structures. Turbulence characteristics differ between the boundary layer, rotor wakes and free flow. Hence also different noise source characteristics are distinguished [1]. In this study, we focus on the influence of stretched turbulence eddies in the free flow that interact with the rotor blades [2].

One method to separate the rotor-incoherent components from the rotor-coherent, phase-locked tones is the cyclostationary analysis [3, 4]. However, the remaining broadband spectrum typically contains very narrow spectral components that may be mistaken as tones. These rotor-incoherent narrowband components have a stochastic phase relation relative to the rotor rotation by definition and appear at and around the blade passing frequencies (BPF). A dominant source of these components are local random pressure fluctuations at the blade leading edges caused by ingested atmospheric turbulence eddies. The eddies are stretched due to the flow acceleration at the fan inlet in ground tests. These elongated structures interact with more than one blade and form a partly correlated noise source [2]. In forward flight no such narrowband noise appears as the turbulence eddies in the atmosphere have small correlation lengths and are not stretched by acceleration [5]. Hence, the turbulence ingestion noise can be modelled as a fully uncorrelated source for most aircraft applications [1]. This is however not the case for modern designs with potentially embedded

engines or in urban air mobility where the take-off and landing conditions may be comparable to ground tests. In this case the correlation length of the ingested eddies can be modelled for the prediction of these partly correlated noise sources [6].

A new acoustic fan test rig was recently commissioned at the DLR to investigate the acoustic and aerodynamic effects of inflow distortion and turbulence ingestion [7]. The test rig has a modular design, allowing comprehensive parameter variations. In the controlled setup advanced analysis methods are applied to estimate turbulence parameters from hot-wire anemometry [8]. The emitted sound power is calculated by means of a radial mode analysis using a combined axial and azimuthal sensor array [9].

In the scope of this study, the purely uncorrelated noise and the partly correlated narrowband noise emitted by a laboratory fan is investigated. To further investigate and understand the fan noise generating mechanisms a parameter variation is conducted at constant rotor speed and various loading conditions. The rotor-incoherent sound power spectrum is split into rotor-incoherent narrowband peaks and broadband noise. The trends of the sound power are investigated for different frequency bands. The scientific question is, whether the narrowband peaks follow a different trend than the overall broadband noise, when the loading is varied.

A honeycomb is mounted in the inlet which reduces the turbulence integral length scale (ILS) while increasing the turbulence intensity. The influence of the Honeycomb on the narrowband and broadband components is investigated for all operating points.

The experimental and simulated results are contrasted. Simulations were performed with a theoretical fan noise prediction model [1]. Estimated turbulence parameters from hot-wire anemometry measurements serve as input parameters for the model. A similar comparison was previously conducted for a different test rig and showed good agreement for the broadband noise [10]. The simulated noise sources are the broadband rotor-stator interaction, the inflow-rotor interaction and the inflow-stator interaction.

This paper is structured as follows: Next section describes the measurement setup, and is followed by a summary of the analysis techniques and measurement results. The results are discussed supported by simulated data.

MEASUREMENT SETUP

The Co-/Contra Rotating Acoustic Fan Test rig CRAFT shown in Figure 1 was designed for fan speed up to 4500 RPM. On the left-hand side of this figure the approx. spherical in-house designed and constructed inflow control device (ICD) with a diameter of 1.25 m is depicted mounted on the inlet [11]. On the right-hand side the measurement section with arrays of wall-flushed mounted microphones up- and downstream of the fan is shown. The flow-stream goes from the right to the left side and the rotation direction is indicated by a red arrow in the rotor plane.

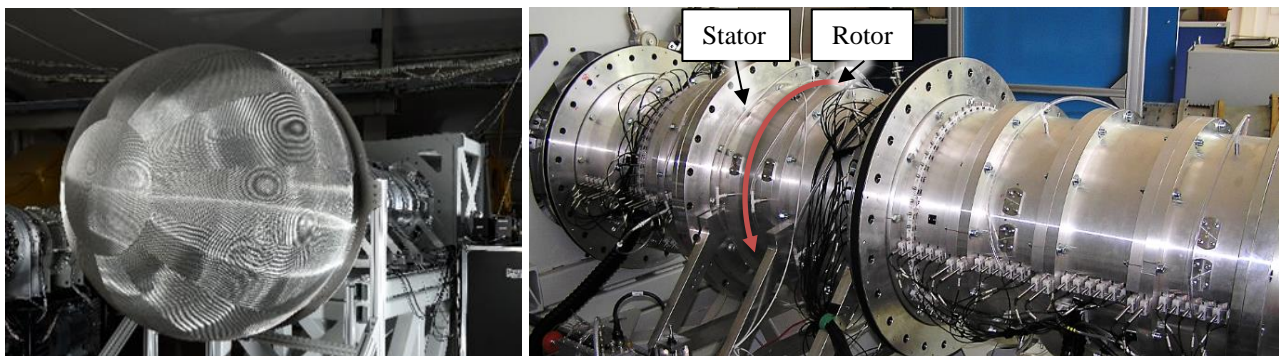


Figure 1: Fan test rig CRAFT: Inflow Control Device, mounted on the inlet (left) and the measurement section with two traversable microphone arrays in the inlet and in the outlet and one fixed ring array in the inlet, downstream of the rotating duct (right).

With the reference fan, a rotor-stator configuration with $B = 18$ rotor blades and $V = 21$ stator vanes, the test rig reaches an axial Mach number of up to 0.14 in the inlet section and 0.2 in the outlet section with hub. The rotor tip Mach number is 0.31 at the design rotor speed. The operating conditions of the fan are adjusted with a Pitot tube in the inlet and circumferentially distributed static pressure holes in the inlet and the outlet section. The fan operating points are set reproducibly under the criterion of Mach number similarity. For this purpose, the mass flow rate and rotation speed are corrected to ISA sea-level conditions in terms of the ambient pressure and temperature. The test rig has a constant duct radius of 226.8 mm with a hub radius of 139 mm in the outlet.

In the scope of this study only data from the microphones upstream of the fan is analyzed. The sensors are arranged in an equidistant ring of 59 microphones 300 mm upstream of the rotor leading edges and a line array of 30 sensors 24 mm apart. Its extremities are 420 mm and 1108 mm upstream of the rotor leading edge. The G.R.A.S. condenser microphones with capsule type 40BP and preamplifier type 26AR have an accuracy of ± 1 dB in the frequency range between 10 Hz and 25 kHz. A sketch of the test rig and a photograph of the setup are shown in Figure 2. The hot-wire measurements were conducted 670 mm upstream of the rotor, as marked by a red ellipse in the photograph in Figure 2. The microphone array can be used for a radial mode analysis up to 6 kHz with high accuracy, as is discussed along with further details on the test rig and its measurement capabilities in [7].

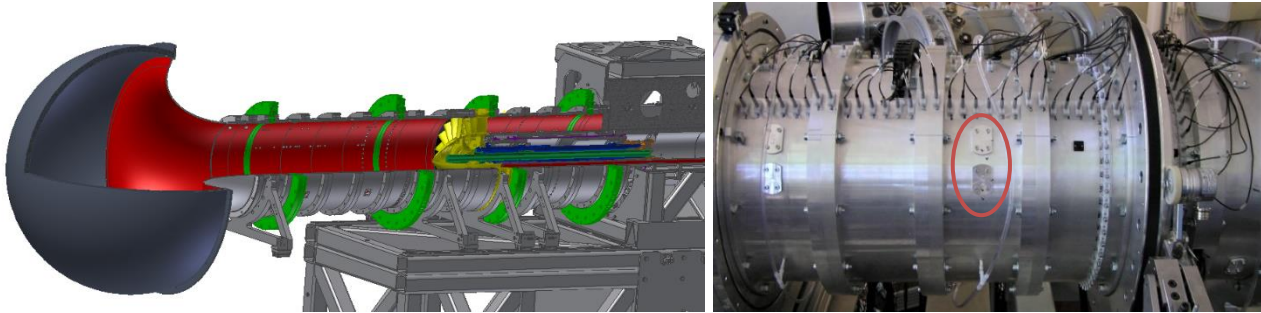


Figure 2: Microphone arrays in the inlet measurement section of the test rig. Left-hand side: Schematic view of the test rig. Right-hand side: Photograph of the mounted microphones. Not used positions are closed with a dummy plug. In both figures the flow-stream goes from the left to the right side.

The 30 s long microphone signals have a sample rate of 65536 Hz.

RADIAL MODES IN ANNULAR DUCTS WITH FLOW

The analysis of the acoustic measurements is based on a modal decomposition of the sound field. The mode shapes are harmonic in the axial and azimuthal direction. In the radial direction the Bessel differential equation is solved with acoustically hard wall boundary conditions. This model assumes a plane flow profile and can also consider a solid body swirl (which is not present in the inlet). The modes are commonly described by means of their azimuthal mode order m and radial mode order n . The sound pressure p at any position in the duct $\mathbf{x} = [x, r, \theta]$ can then be expressed as a sum of modes:

$$p(\mathbf{x}) = \sum_{m=-\infty}^{\infty} \sum_{n=0}^{\infty} (A_{mn}^+ e^{ik_{mn}^+ x} + A_{mn}^- e^{ik_{mn}^- x}) f_{mn}(r) e^{im\theta}. \quad (1)$$

With A_{mn}^+ and A_{mn}^- denoting the complex amplitude of the mode propagating in the downstream (+) or upstream direction (-), respectively. The propagation in the axial direction is described by the axial wavenumber k_{mn}^+ and k_{mn}^- respectively. The radial mode shape function $f_{mn}(r)$ is described in reference [9]. The downstream and upstream propagating sound power is the sum of the respective

modal powers: $P^\pm = \sum_m \sum_n P_{mn}^\pm$. The sound power of each mode P_{mn}^\pm is calculated using the formulation of Morfey [12]:

$$P_{mn}^\pm = \frac{\pi R^2 \alpha_{mn} (1 - M_x^2)^2}{\rho c (1 \mp \alpha_{mn} M_x)^2} |A_{mn}^\pm|^2, \quad (2)$$

where R denotes the ducts radius, ρ the air density, c the speed of sound, M_x the axial Mach number, and $\alpha_{mn} = [1 - (1 - M_x^2)(\sigma_{mn}/kR)^2]^{0.5}$ the mode propagation factor. This factor is equal to zero for cut-off frequencies and approaches the unity far above the cut-on frequency border.

A method proved to be useful for uncorrelated sound fields is the combined axial and azimuthal sensor array (CAAS) method [9]. It is based on the cross spectral densities between each sensor in the ring array and every sensor in the line array. Before the application of mode analysis, the rotor-coherent sound field is filtered by means of a cyclostationary analysis [3, 4]. For this purpose, the signals are resampled using the rotor trigger, to compensate for rotor speed variations. From the resampled signal the rotor-coherent and rotor-incoherent spectra are calculated using exactly 8 rotor revolutions per window resulting in a resolution of approximately 9.4 Hz or 1/8th engine order [4]. Ideally, by this the sound field is completely split into rotor-coherent tonal components and rotor-incoherent broadband components. However, partly correlated narrowband components caused by the interaction of the rotor with large-scale turbulent structures remain in the rotor-incoherent spectrum, as described by Hanson [2] and Atassi *et al.* [13]. Turbulent pressure fluctuations, which can be significant at low frequencies, are not filtered by the CAAS method either. In order to investigate the sound power in these narrowband components separately from the broadband components a simple filtering technique is used. As a first step the sound power spectrum is integrated over frequency bands around each engine order. The signal was primarily resampled and the sound power of each band $P(eo)$ can be calculated as the sum of exactly 8 frequency bins per band. The narrowband component at the h -th BPF harmonic is estimated as:

$$\hat{P}_h = P(hB) - 0.5(P(hB + 1) + P(hB - 1)). \quad (3)$$

The broadband spectrum is the difference between the integrated overall spectrum and the narrowband components $\bar{P}(eo) = P(eo) - \hat{P}(eo)$. The broadband spectrum is again summed over frequency bands around each BPF with a bandwidth equivalent to the blade passing frequency as \bar{P}_h .

RESULTS

Figure 3 shows the auto power spectrum averaged over 59 microphones in the ring array with the filtered rotor-coherent and rotor-incoherent components. Fan operation point was close to design conditions: rotor speed $N = 4500 \text{ RPM}_c$ (ISA sea-level corrected value of RPM) and flow coefficient $\Phi := M_x/M_{tip} = 0.33$. The turbulence generated by the ICD is accelerated and stretched in the inlet bell mouth. Therefore, narrowband noise is measured at the BPF harmonics in the green rotor-incoherent spectrum, typically these are more relevant at the lower BPF harmonics [2].

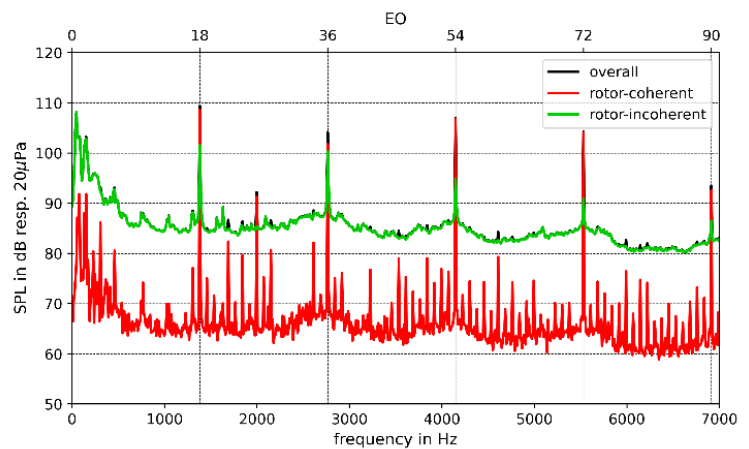


Figure 3: Overall auto power spectrum averaged over all microphones in the ring array together with the rotor coherent and rotor-incoherent components.

Figure 4 illustrates the result of a radial mode analysis with the CAAS method. The sound power of all upstream propagating modes with the same azimuthal order are summed to compute the modal sound power $P_m^- = \sum_n P_{mn}^-$. The left-hand side plot in Figure 4 refers to the operating point $N = 4500 \text{ RPM}_c$ and $\Phi = 0.33$ (same as in Figure 3), whereas on the right-hand side plot it is close to the surge line $N = 4500 \text{ RPM}_c$ and $\Phi = 0.26$. The problem is well conditioned for frequencies up to about 6 kHz (or engine order 80 at this fan speed) [7]. Beyond this range, modes with small azimuthal mode order are poorly reproduced. This effect is visible in the results as a strong overestimation of the modal amplitudes. At low frequencies, below 500 Hz or engine order 7, turbulent pressure fluctuations dominate the spectrum. The modal sound power is generally higher for modes with lower mode orders, as these have a higher propagation factor. For the operating point with small flow coefficient, the modal spectrum is asymmetric, and more sound power is concentrated in the modes with negative spinning direction. This is expected as the overall dominating rotor-stator interaction noise source increases when the flow coefficient decreases. Two effects explain the asymmetry of this source: On the one hand, the noise sources on the stator leading edge are dipole-like and radiate more efficiently in the negative θ -direction [10]. On the other hand, in the coordinate system used, the direction of fan rotation is negative (counter-clockwise). Therefore, modes with positive spinning direction originating from the stator are stronger shielded by the rotor [14]. Between BPF and 2 BPF distinct mode amplitudes are visible. These sound field components are out of the scope of the analysis here, but will be investigated in further studies.

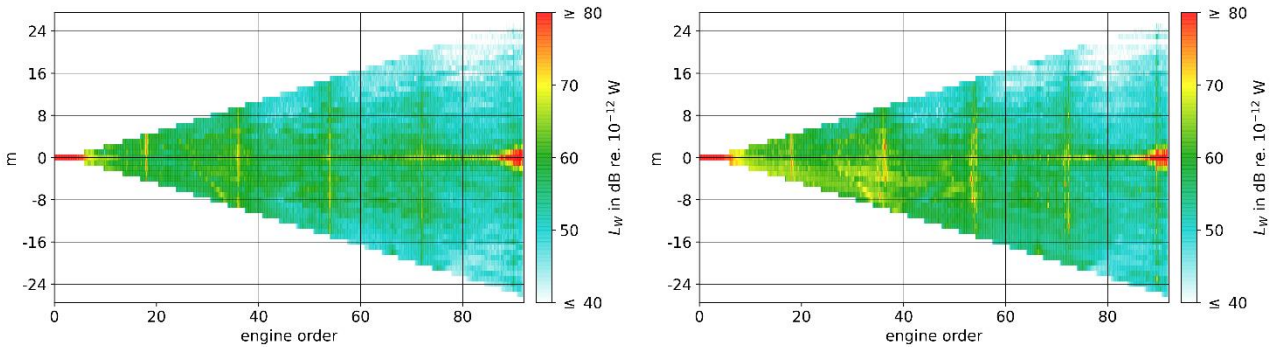


Figure 4: Modal sound power P_m (summed over n) close to aerodynamic design point (left) and with maximum loading close to surge (right).

Figure 5 shows the sum of the modal powers with 8 frequency bins per engine order, comparing the upstream and downstream propagating sound powers. The same operating points are shown with $N = 4500 \text{ RPM}_c$ and $\Phi = 0.33$ on the left and $\Phi = 0.26$ on the right, respectively. For the higher loading condition ($\Phi = 0.26$), the upstream propagating sound power is increased, especially at frequencies between BPF and 3 BPF, when compared against the lower loading condition case ($\Phi = 0.33$). The downstream propagating sound power remains at the same level for both operating points. Therefore, the power difference between up- and downstream components is even higher for the high loading case. This suggests that the upstream propagating sound power that is emitted from the fan can be separated from reflections at the inlet and other noise sources that are not related to the fan stage.

It is worth mentioning that for the operating point close to surge ($\Phi = 0.26$), the narrowband peaks are observed slightly above and below the 2nd, 3rd and 4th BPF harmonics. This noise source might be related to large turbulence structures generated by a possible flow separation at the rotor blades. This hypothesis should be validated by examination of the turbulence properties measured behind the rotor with hot-wire probes.

Figure 6 depicts the integrated sound power spectra around each engine order of the two operating points as described above. The grey curve is the overall rotor-incoherent sound power whereas the green curve is the broadband sound power $\bar{P}(eo)$. The green diamonds denote the narrowband sound powers at the BPF harmonics \hat{P}_h .

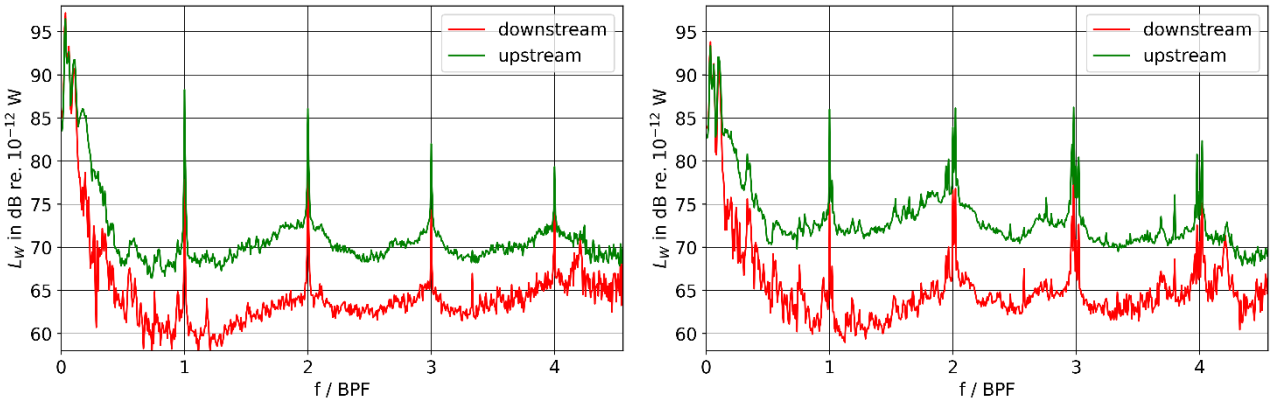


Figure 5: Sound power spectrum close to aerodynamic design point (left) and with maximum loading close to surge (right).

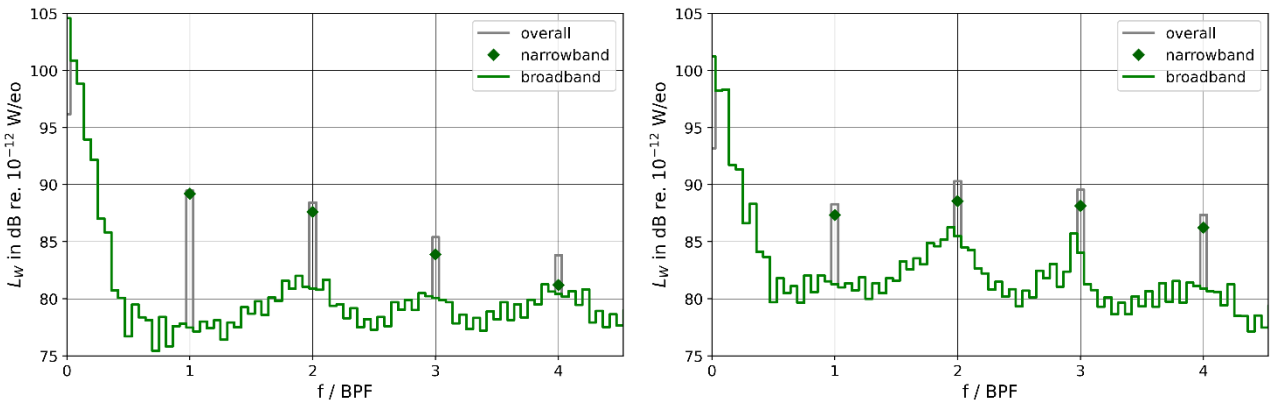


Figure 6: Upstream propagating rotor-incoherent sound power level per engine order with separation into narrowband and broadband components close to aerodynamic design point (left) and with maximum loading close to surge (right).

Figure 7 shows the comparison of the sound power levels P_h of the narrowband and broadband components of the first 4 BPF harmonics. The subscript h indicates the BPF harmonic order. In this plot the circles denote the broadband power, whereas the diamonds the narrowband power. The trends of the narrowband components (diamonds) show no strong dependency of the loading.

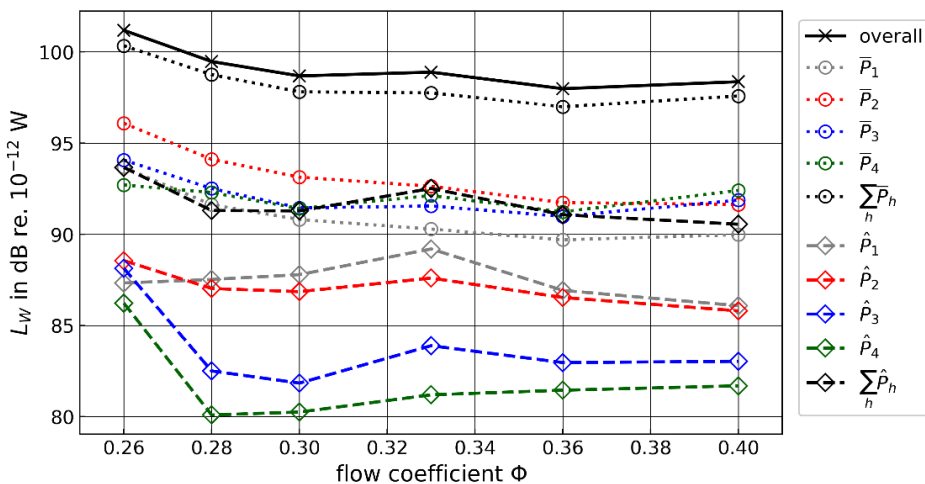


Figure 7: Variation of sound power levels of rotor-incoherent broadband and narrowband around 1BPF to 4BPF with fan loading. Configuration without flow straightener honeycomb.

For the 1st and 2nd harmonics, the levels vary a few dB among the operating points. For the 1st harmonic, the power level reaches a maximum at $\Phi = 0.33$. For the 2nd harmonic however, this maximum is found at $\Phi = 0.26$. The sound power of the narrowband components around 3rd and

4th harmonic slightly increases from $\Phi = 0.28$ to $\Phi = 0.40$, but have a pronounced increase of about 6 dB from $\Phi = 0.26$ to $\Phi = 0.28$. This strong increase of sound power is driven by the narrowband peaks beside these BPF harmonics. In general, the narrowband components become less relevant at higher BPF harmonics. This is also described by Hanson for the partly correlated noise source due to elongated eddies [2].

The broadband sound power (denoted by circles) around the 1st and 2nd BPF decreases about 4 dB from $\Phi = 0.26$ to $\Phi = 0.40$. The sound power around 3rd and 4th BPF varies only slightly between the operating points. However, the sound power around the 4th BPF (green circles) is the lowest at maximum loading, but highest at maximum flow rate. The curve with black circles denotes the summed broadband sound power of the engine orders 9 to 81, neglecting the high amplitudes at low frequencies. The overall spectrum also contains the narrowband spectra which make a difference of about 1 dB at all operating points compared to the pure broadband sound power.

In Figure 8 the results of the same analysis chain are shown, but applied to a different setup where a flow straightening honeycomb was inserted downstream the bell mouth. The honeycomb is 25 mm thick and has hexagonal cell size of 6.25 mm. This device induces additional flow turbulence that is not accelerated and therefore not stretched in axial direction. Hot-wire anemometry measurements have shown that the turbulence levels behind the honeycomb is slightly increased (from approx. 0.2 % to 0.5 %), but the ILS of this flow-field is reduced from the magnitude of 100 mm to 3 mm outside the boundary layer. The turbulence properties approximate more to an isotropic condition due to this honeycomb while the turbulent boundary layer thickness in the duct is not affected. The turbulence analysis results are not shown as they are outside the scope of the present paper.

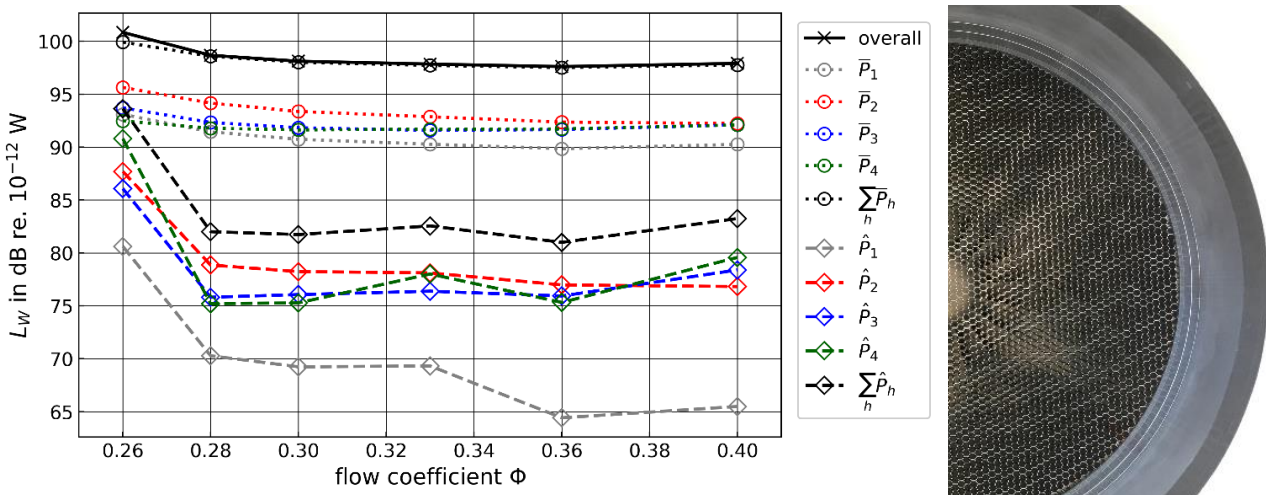


Figure 8: Variation of sound power levels of rotor-incoherent broadband and narrowband around 1BPF to 4BPF with fan loading. Configuration with flow straightener honeycomb downstream of the bell mouth inlet and upstream of the measurement section as shown in the right figure.

The trends of the broadband components are virtually not affected by the honeycomb. The sound power of the broadband noise is increased, but not as much as one might expect with almost double turbulence intensity. Possibly the effects due to increased Tu are masked by the rotor-stator interaction. The narrowband components show a reduction of more than 10 dB for all operating points, except for the point close to surge. This result suggests that narrowband components arise from anisotropic stretched ingested turbulence. Strong narrowband components arise close to surge in this configuration as well. This supports the hypothesis from above, that a flow separation at the blades generates large turbulence structures at this blade loading.

COMPARISON WITH SIMULATED RESULTS

The used theoretical fan noise prediction model is based on the extended acoustic analogy by Goldstein [15] for sources with moving solid boundaries. On the basis of a semi-empirical

approach, the aerodynamic properties are calculated for a mean line and radially extrapolated [1]. Important input parameters of this model are the turbulence intensity $Tu = \tilde{u}_x/U_x$ in the axial direction and the ILS. The turbulence is assumed to be homogenic and isotropic in the analytical model. Tu and ILS are determined by means of hot-wire anemometry measurements at 25 radial positions and a fit to a von-Kármán spectrum [8]. To calculate an acoustically equivalent turbulence intensity, the determined values are weighted with the relative steady velocities at the respective radius:

$$Tu = \int_0^R Tu(r)(U_x^2 + U_{tip}^2 \frac{r}{R}) dr / \int_0^R (U_x^2 + U_{tip}^2 \frac{r}{R}) dr, \quad (4)$$

where U_x is the axial flow speed and U_{tip} the rotor tip speed. By applying this averaging, a value of $Tu = 1.0 \%$ is obtained. In the simulation a constant turbulence intensity is assumed. However, the turbulence kinetic energy $TKE = 3\tilde{u}^2/2$ scales with the axial flow speed and varies from $0.12 m^2/s^2$ at maximum loading ($\Phi = 0.26$) to $0.29 m^2/s^2$ at maximum flow rate ($\Phi = 0.40$). The assumption of constant Tu was confirmed by means of a measurement at 50 % rotor speed. The ILS is weighted with the TKE at the respective radius to consider mainly turbulent structures that contain the most energy. An estimate value of $ILS = 0.1 m$ is obtained for the modeling.

Figure 9 depicts on the left-hand side the result of the upstream propagating broadband noise emitted by rotor-stator interaction, inflow-rotor interaction, inflow-stator interaction, and trailing edge noise (TE). The same flow coefficients as in the measurements are depicted. The rotor-stator interaction broadband noise decreases about 20 dB with increasing flow rate. This noise source is especially high at high fan loading because here the rotor wakes are large due to the stronger flow deceleration across the blade row, thus generating more turbulence impinging onto the stator vanes [16].

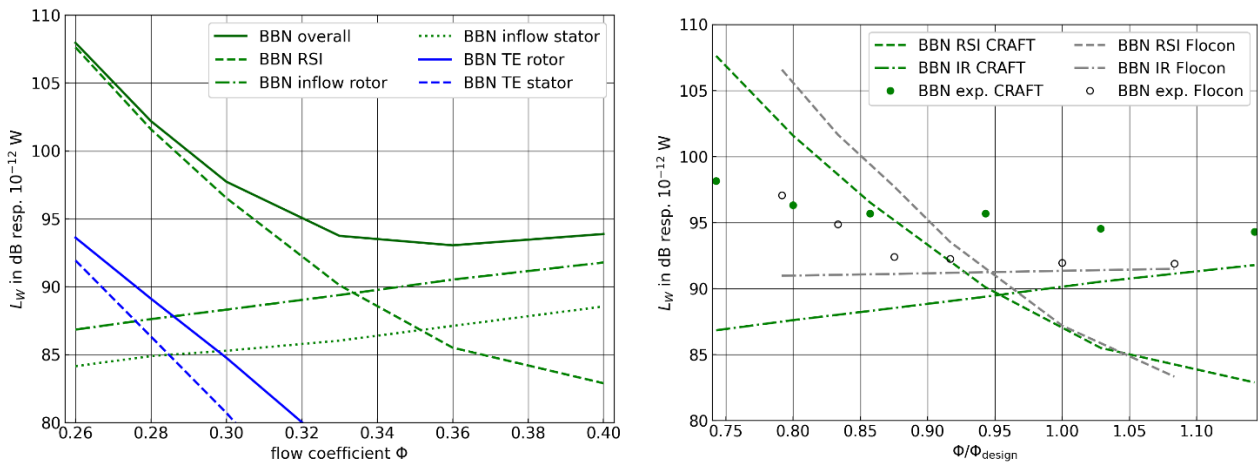


Figure 9: Simulations of different noise sources at the CRAFT test rig. On the left the contributions of different broadband noise sources calculated using the analytical fan noise prediction model are shown. On the right a comparison with measurements and scaled broadband noise from different test rigs CRAFT and Flocon is shown.

The rotor trailing edge noise has a similar evolution as it also is driven by the size of the rotor wakes. This source dominates the stator trailing edge noise due to the higher flow velocity at which the turbulent structures are convected past the rotor trailing edge compared to that of the stator vanes.

The inflow rotor noise is steadily increased with the flow rate. This source mechanism is mostly driven by the TKE of incoming inflow turbulence. As we assume a uniform value for Tu the TKE scales directly with the axial flow speed.

The simulated sound power level is overestimated at low flow rates, where the rotor stator interaction is modeled as the dominant noise source, when compared with the experimental data.

The rotor stator interaction noise is calculated at the noise source in the interstage area. Note, that propagation effects such as mode scattering and shielding by the rotor are not considered in the simulation. An estimation of these effects could be object of further studies.

On the right-hand side of Figure 9, the simulation and experimental results are compared to a similar simulation performed to a different test rig named Flocon. This test rig has the same duct radius, but lower design fan speed $N = 3200$ RPM and smaller flow coefficients: from $\Phi = 0.19$ to $\Phi = 0.26$ [10]. To compare the results of the different test rigs, the flow rates are normalized to the flow rate at the respective design points: $\Phi = 0.35$ for the CRAFT and $\Phi = 0.24$ for the Flocon rig. The sound power level of the Flocon rig is scaled with the rotor speed $L_{W, scaled} = L_W + 50 \log_{10}(4500/3200)$. The tests at the Flocon rig were measured with a different array, that allowed sound power calculations up to the engine order 37. Therefore integrated results up to this engine order are compared.

The aerodynamic performance of the two test rigs is rather different. For example, the efficiency of the CRAFT test rig is higher over a wider range of flow coefficients, which was a design criterium of the rotor-stator stage [7]. This could explain why the decrease of the simulated rotor-stator interaction noise and the measured broadband noise is more pronounced for the Flocon test rig. This should also be validated by means of hot-wire measurements in the inter-stage section. The scaled inflow-rotor noise of the Flocon test rig is higher than that of the CRAFT. This can partly be explained by a higher inflow turbulence. At the Flocon test rig an earlier and less well optimized design of the ICD was used, which left a higher remaining turbulence intensity of $Tu \approx 1.2$ %. This value was used for the simulations of the Flocon rig.

CONCLUSION AND FUTURE WORK

The rotor-incoherent broadband and narrowband noise characteristics of a new fan test rig are investigated for a variation of blade loading. The narrowband components predominantly arise from stretched anisotropic ingested turbulence that interact with multiple blades. As a result, it creates partly correlated noise sources which seem not to have a clear dependency on the fan loading. This hypothesis is ratified by measurements conducted with an additional honeycomb installed downstream of the bell mouth inlet. Besides reducing lateral turbulence and increasing the axial turbulence, the presence of this honeycomb reduces the integral length scale. As a result, the narrowband noise components around the BPF tones are remarkably reduced.

At the lowest flow coefficient (close to the surge line) narrowband peaks alongside with the BPF harmonics are observed as a different source mechanism which leads to a remarkable increase in the narrowband sound power at this operation condition. This effect is also observed in the configuration with the honeycomb installed and will be an object of further studies.

The broadband components around the 1st and 2nd BPF resemble the trends of the broadband rotor stator interaction: A decrease in sound power with increasing flow coefficient. This effect is not as pronounced as in simulations with the prediction model.

The results are successfully compared with experimental and simulated data from a different test rig with comparable dimensions but a different blade design. The variation of the simulated dominant rotor-stator interaction noise is smaller for the CRAFT test rig. The experimentally determined overall rotor-incoherent sound power emission varies less for the CRAFT as well. This is also expected because the rotor of the CRAFT test rig was designed with the condition of a wide operating range in terms of incidence angles.

Future work comprises the extension of this study concerning the analysis of the fan tones and analyses of both rotor-coherent and rotor-incoherent sound components in the fan outlet. The results will also be used as reference for measurements with inflow distortions that are representative for different fan installations.

BIBLIOGRAPHY

- [1] A. Moreau – *A unified analytical approach for the acoustic conceptual design of fans of modern aero-engines*. PhD Thesis, Technical University Berlin, DLR research report DLR-FB-2017-56, **2017**.
- [2] D. B. Hanson – *Spectrum of rotor noise caused by atmospheric turbulence*. The Journal of the Acoustical Society of America 56, pp. 110-126, **1974**.
- [3] J. Antoni – *Cyclostationarity by examples*. Mechanical Systems and Signal Processing, Vol. 23, No. 4, pp. 987 – 1036, **2009**.
- [4] M. Behn, B. Pardowitz, U. Tapken – *Separation of Tonal and Broadband Noise Components by Cyclostationary Analysis of the Modal Sound Field in a Low-Speed Fan Test Rig*. fan2018 International Conference on Fan Noise, Aerodynamics, Applications and Systems, Paper-nr. 043, Darmstadt, Germany, **2018**.
- [5] J. S. Preisser, D. Chestnutt – *Flight effects on fan noise with static and wind-tunnel comparisons*. Journal of Aircraft 21.7, pp. 453-461, **1984**.
- [6] M. Staggat – *Modellierung und Prognose des Grenzschicht-Rotor-Interaktionschalls für integrierte Triebwerke*, Ph.D Thesis, Technical University Berlin, **2021**.
- [7] U. Tapken, L. Caldas, R. Meyer, M. Behn, L. Klähn, R. Jaron, A. Rudolphi – *Fan test rig for detailed investigation of noise generation mechanisms due to inflow disturbances*. AIAA Aviation 2021 Forum, August 2-6, Virtual Event, **2021**.
- [8] L. Caldas, C. Kissner, M. Behn, U. Tapken, R. Meyer – *Comparison of Techniques for the Estimation of Flow Parameters of Fan Inflow Turbulence from Noisy Hot-Wire Data*. Fluids, 6, 372, **2021**.
- [9] U. Tapken, D. Gutsche, L. Enghardt – *Radial mode analysis of broadband noise in flow ducts using a combined axial and azimuthal sensor array*. 20th AIAA/CEAS Aeroacoustics Conference, Atlanta, GA, USA, AIAA 2014-3318, **2014**.
- [10] L. Klähn, A. Moreau, L. Caldas, R. Jaron, U. Tapken – *Advanced analysis of fan noise measurements supported by theoretical source models*. International Journal of Aeroacoustics, accepted for publication **2021**.
- [11] L. Caldas, S. Oertwig, A. Rudolphi, R. Meyer, L. Enghardt U. Tapken – *Development and assessment of an inflow control device and a bell-mouth for a low-speed aeroacoustic fan rig*. 25th AIAA/CEAS Aeroacoustics Conference, Delft, The Netherlands, AIAA 2019-2713, **2019**.
- [12] C. Morfey – *Sound transmission and generation in ducts with flow*. Journal of Sound and Vibration, Vol. 14, No. 1, pp. 37-55, **1971**.
- [13] H. Atassi, M. Logue – *Fan Broadband Noise in Anisotropic Turbulence*. 15th AIAA/CEAS Aeroacoustics Conference, Miami, Florida, AIAA 2009-3148, **2009**.
- [14] D. B. Hanson – *Acoustic reflection and transmission of 2- dimensional rotors and stators including mode and frequency scattering effects*. Research report NASA/CR-1999-208880, NASA, Glenn Research Center, **1999**.
- [15] M. Goldstein – *Unified approach to aerodynamic sound generation in the presence of solid boundaries*. Journal of the Acoustical Society of America, 56, pp. 497-509, **1974**.
- [16] B. Lakshminarayana, T. R. Govindan. B. Reynolds – *Effects of rotation and blade incidence on properties of turbomachinery rotor wake*. AIAA Journal 20(2), pp. 245–253, **1982**.